Charge density wave instability and pressure-induced superconductivity in bulk $1T$-NbS_2

Wei Wang,[1] Bosen Wang,[2] Zhibin Gao,[3] Gang Tang,[4] Wen Lei,[1] Xiaojun Zheng,[1] Huan Li,[1] Xing Ming,[1,*] and Carmine Autieri[5,†]

[1]*College of Science, Guilin University of Technology, Guilin 541004, China*
[2]*Beijing National Laboratory for Condensed Matter Physics and Institute of Physics, Chinese Academy of Sciences, Beijing 100190, China*
[3]*Department of Physics, National University of Singapore, Singapore 117551, Republic of Singapore*
[4]*Theoretical Materials Physics, Q-MAT, CESAM, University of Liège, B-4000 Liège, Belgium*
[5]*International Research Centre MagTop, Institute of Physics, Polish Academy of Sciences, Aleja Lotników 32/46, PL-02668 Warsaw, Poland*

(Received 3 April 2020; revised 15 September 2020; accepted 16 September 2020; published 13 October 2020)

Charge density wave (CDW) instability and pressure-induced superconductivity in bulk $1T$-NbS_2 are predicted theoretically by first-principles calculations. We reveal a CDW instability toward the formation of a stable commensurate CDW order, resulting in a $\sqrt{13} \times \sqrt{13}$ structural reconstruction featured with star-of-David clusters. The CDW phase exhibits one-dimensional metallic behavior with in-plane flatband characteristics and coexists with an orbital-density-wave order predominantly contributed by the $4d_{z^2-r^2}$ orbital from the inner Nb atoms of the star-of-David cluster. By doubling the cell of the commensurate CDW phase along the layer stacking direction, a metal-insulator transition may be realized in the CDW phase in cases where the interlayer antiferromagnetic ordering and Coulomb correlation effect have been considered simultaneously. Bare electron susceptibility, phonon linewidth, and electron-phonon coupling calculations suggest that the CDW instability is driven by softened phonon modes due to the strong electron-phonon coupling interactions. CDW order can be suppressed by pressure, concomitant with the appearance of the superconductivity. Our theoretical predictions call for experimental investigations to further clarify the transport and magnetic properties of $1T$-NbS_2. Furthermore, it would also be very interesting to explore the possibility to realize the CDW order coexisting with the superconductivity in bulk $1T$-NbS_2.

DOI: 10.1103/PhysRevB.102.155115

I. INTRODUCTION

Quasi-two-dimensional (2D) layered transition-metal dichalcogenides (TMDCs) have attracted extensive attention in recent years. TMDC materials often crystallize in $1T$ or $2H$ polymorph with octahedral or trigonal prismatic coordination [1]. Many group-V TMDC materials MX_2 (M denotes the transition metals Nb or Ta, and X stands for the chalcogen elements Se or S) exhibit interesting phenomena and properties, such as charge density wave (CDW) order, superconductivity, metal-insulator transitions, magnetic ordering, and Mott physics [2–13]. However, even though possessing the same MX_2 chemical composition, different polytypes of MX_2 exhibit completely different physical properties. For example, $1T$ polymorphs of TaS_2 and $TaSe_2$ show complex CDW phase diagrams, including incommensurate, nearly commensurate, and commensurate CDW (CCDW) phases with prototypical $\sqrt{13} \times \sqrt{13}$ star-of-David structural reconstructions upon decreasing temperature [2,13,14]. Electronic structure transitions arising from the Mott-Hubbard physics is observed in the CCDW phase of $1T$-TaS_2 [13], whereas the Mott insulating phase does not appear in bulk $1T$-$TaSe_2$ even in the CCDW state [14]. In addition, the CDW instability in $1T$ polymorphs of TaS_2 and $TaSe_2$ can be suppressed under high pressure, and then the associated superconductivity emerges [13,15–19]. By contrast, the CDW order and superconductivity can coexist in the $2H$-MX_2, exhibiting complicated competitive or cooperative relations [4,20–22]. Furthermore, the CDW phase transitions display a 3×3 periodicity in the bulk form of $2H$-MX_2 [4,11,12]. However, previous research indicates that $2H$-NbS_2 does not exhibit CDW order due to anharmonic suppression [23,24]. Recent experiments observe very weak superlattice peaks in $2H$-NbS_2 corresponding to a commensurate $\sqrt{13} \times \sqrt{13}$ periodic lattice distortion, identical to the cases in $1T$ polymorphs of TaS_2 and $TaSe_2$, which may be stem from a local $1T$-like environment in the $2H$ crystal arising from stacking faults [25].

In addition to the significant roles of the different polymorphs, the dimensionality also plays a profound impact on the transport properties, CDW order, and superconductivity of MX_2. The CDW phase of the monolayer $1T$-$TaSe_2$ is identified to be a Mott insulator with an unusual orbital texture; however, the energy gap reduces significantly for the bilayer, while the trilayer and the bulk show a semimetallic and one-dimensional (1D) metallic behavior, respectively [14,26,27]. Contrary to the bulk phase, a 3×3 CDW order has been observed in the single-layer $2H$-NbS_2; however, it is so fragile that it can be disturbed by small compressive strains [28–30]. Strain-induced phase separation between triangular and stripe

*mingxing@glut.edu.cn
†autieri@magtop.ifpan.edu.pl

phases in charge-ordered $1H$-$NbSe_2$ monolayer has been explored by *ab initio* calculations [31]. Compared to the bulk $2H$ polymorph of $NbSe_2$ and $TaSe_2$, the CDW instability can be strongly enhanced in their monolayer [32,33]. By contrast, the CDW order of bulk $2H$-TaS_2 vanishes in the 2D monolayer limit, accompanied with a substantial enhancement of the superconductivity, indicating a competition between CDW order and superconductivity [34,35]. Although it is difficult to synthesize bulk $1T$ polymorph of $NbSe_2$ and NbS_2, few-layer thin films and monolayers have been prepared successfully [36–39]. Similar to other $1T$ polytype CDW materials, the monolayer $1T$-$NbSe_2$ is found to be a Mott insulator concomitant with the typical $\sqrt{13} \times \sqrt{13}$ CDW order [38–41], and the monolayer $1T$-NbS_2 is predicted theoretically to undergo a $\sqrt{13} \times \sqrt{13}$ star-of-David structural reconstruction stabilized in a spin-1/2 magnetic insulating state [42].

The purpose of the present paper is to further explore the existence of CDW instability in bulk $1T$-NbS_2 by first-principles calculations. We discover that the undistorted high-symmetry $1T$-NbS_2 is unstable with softening phonon modes and undergoes a $\sqrt{13} \times \sqrt{13}$ structural reconstruction to form a stable CCDW phase. Electronic structure calculations indicate that an orbital density wave (ODW) coexists with the CDW order in the CCDW phase featured with flat-band and 1D metallic characteristics. Once the interlayer antiferromagnetic (AFM) ordering and the on-site Coulomb repulsion interactions are taken into account simultaneously, a metal-insulator transition may be observed. By analyzing the Fermi-surface nesting function and calculating the electron-phonon coupling (EPC) constants, we propose that the CDW instability mainly arises from the strong electron-phonon interactions. The CDW order can be suppressed under high pressure, accompanied by the emergence of the superconductivity in the compressed phase. Further experimental and theoretical investigations on the structure and transport behavior of $1T$-NbS_2 under pressure are necessary to better understand the intricate competitive or cooperative relations between CDW order and superconductivity in this material.

II. COMPUTATIONAL DETAILS

The density functional theory (DFT) calculations were performed using the QUANTUM ESPRESSO package [43] with a generalized gradient approximation (GGA) according to the Perdew-Burke-Ernzerhof (PBE) functional [44]. The ultrasoft pseudopotentials were used to describe the interactions between electrons and ionic cores [45]. An energy cutoff of 45 Ry (540 Ry for the charge density) was chosen for our calculations. Considering the 2D layered structure of the bulk $1T$-NbS_2, we performed geometrical optimization with van der Waals (vdW) corrections of DFT-D3 to obtain accurate lattice constants consistent with experiments [46]. The Brillouin zone (BZ) was segmented by a $16 \times 16 \times 8$ Monkhorst and Pack (MP) grid for undistorted high-symmetry $1T$-NbS_2, while a $4 \times 4 \times 8$ MP grid was used for the CCDW structure [47]. The total energy and electron charge density calculations were performed by a Gaussian smearing method with a smearing parameter σ of 0.01 Ry. Using density functional perturbation theory, phonon dispersion curves and EPC were calculated on a $8 \times 8 \times 4$ q grid, and a denser $32 \times 32 \times 16$ k mesh was used for electron-phonon calculation for undistorted structures [48]. Electronic structures and density of states (DOS) are calculated by the Vienna *ab initio* simulation package (VASP) [49,50] within the GGA approach [44] and projector-augmented wave (PAW) potentials [51], where an energy cutoff of 520 eV was used. Because the electronic correlations and band gap are often underestimated in traditional DFT, the adding of a Coulomb correction in the energy functional produces an electronic structure scenario closer to the experimental observation. To more accurately describe the electronic correlations, we perform the first-principles electronic structure calculations also in GGA + U, where an on-site Coulomb interaction U with a value of 2.95 eV was considered for the Nb $4d$ shell [40]. The Fermi surfaces are visualized using the FERMISURFER code [52].

III. RESULTS AND DISCUSSION

A. Undistorted high-symmetry structure of $1T$-NbS_2

As illustrated in Fig. 1(a), bulk $1T$-NbS_2 displays a layered structure with space group $P\bar{3}m1$, and its corresponding BZ and high-symmetry points are illustrated in Fig. 1(b). Each Nb atom is surrounded by six nearest-neighbor S atoms with octahedral coordination, where the adjacent layers are held together by vdW forces. $1T$-NbS_2 film has been synthesized successfully by atmospheric-pressure chemical vapor deposition at 600 °C with lattice parameters $a = 3.4206$ Å and $c = 5.9381$ Å [36]. Our optimized lattice parameters ($a = 3.365$ Å and $c = 5.954$ Å) are in good agreement with the experimental data.

To obtain fundamental features of the electronic structure of the high-symmetry phase, we calculate the band structure and the Fermi surface of the bulk $1T$-NbS_2. As shown in Fig. 2, the electronic structure exhibits similar characteristics with other $1T$ polymorph MX_2 materials [53–55]. The bands around the Fermi energy (E_F) are dominantly contributed by Nb-$4d$ orbitals, which are separated from the S-$3p$ states by a gap of about 0.5 eV below the E_F [Fig. 2(a)]. Due to the quasi-2D nature of the layered structure, the two bands around the gap are nearly flat along the Γ-A direction. Consistent with the octahedral crystal-field splitting, the five $4d$ orbitals are split into triply degenerate t_{2g} ($d_{x^2-y^2}$, $d_{z^2-r^2}$, d_{xy}) and doubly degenerate e_g (d_{yz}, d_{xz}) orbitals [40,42]. The bandwidths of the t_{2g} (~3.5 eV) and e_g (~3 eV) bands are rather large, which implies moderate electron-electron interactions [13]. Specifically, the t_{2g} bands crossing the E_F are occupied by one $4d$ electron, forming 2D electron pockets around the M point. Similar to other $1T$-MX_2, the Fermi-surface features with sixfold petal structural sheets and weak dispersion along the k_z direction [Fig. 2(b)] clearly reflects the quasi-2D nature of the electronic states, which is consistent with the layered structure of $1T$-NbS_2 [53–55].

Generally, it is an effective method to predict the CDW instability by first-principles phonon calculation [15,16,41,56,57]. The phonon spectra of the bulk $1T$-NbS_2 are presented in Fig. 2(c). The phonon instability locating at a distinctive position is believed to be directly related to the CDW distortion, which exhibits softened phonon modes with imaginary frequency at the CDW vector ($\boldsymbol{q}_{cdw}$). The

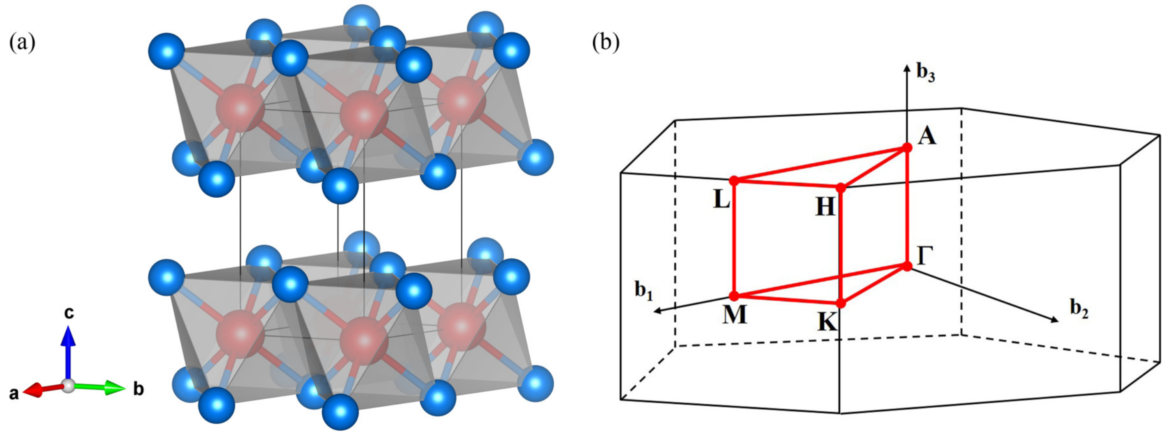

FIG. 1. (a) Crystal structure of the $1T$-NbS_2 bulk and (b) its corresponding BZ. Nb and S atoms are respectively drawn by red and blue balls in (a). The irreducible BZ and high-symmetry points are indicated in (b), where the **Γ** point is at the zone center.

imaginary phonon frequency at $\boldsymbol{q}_{\rm cdw}$ signifies structure reconstructions with a superlattice vector of $\boldsymbol{q}_{\rm cdw}$ [2]. Furthermore, the distributions of phonon frequencies at the plane of $q_z = 0$ in reciprocal space [Fig. 2(d)] confirms that the center of CDW instability is located definitely between **Γ** and **M** at $\boldsymbol{q}_{\rm cdw}$. The CDW instabilities of group-V dichalcogenides MX_2

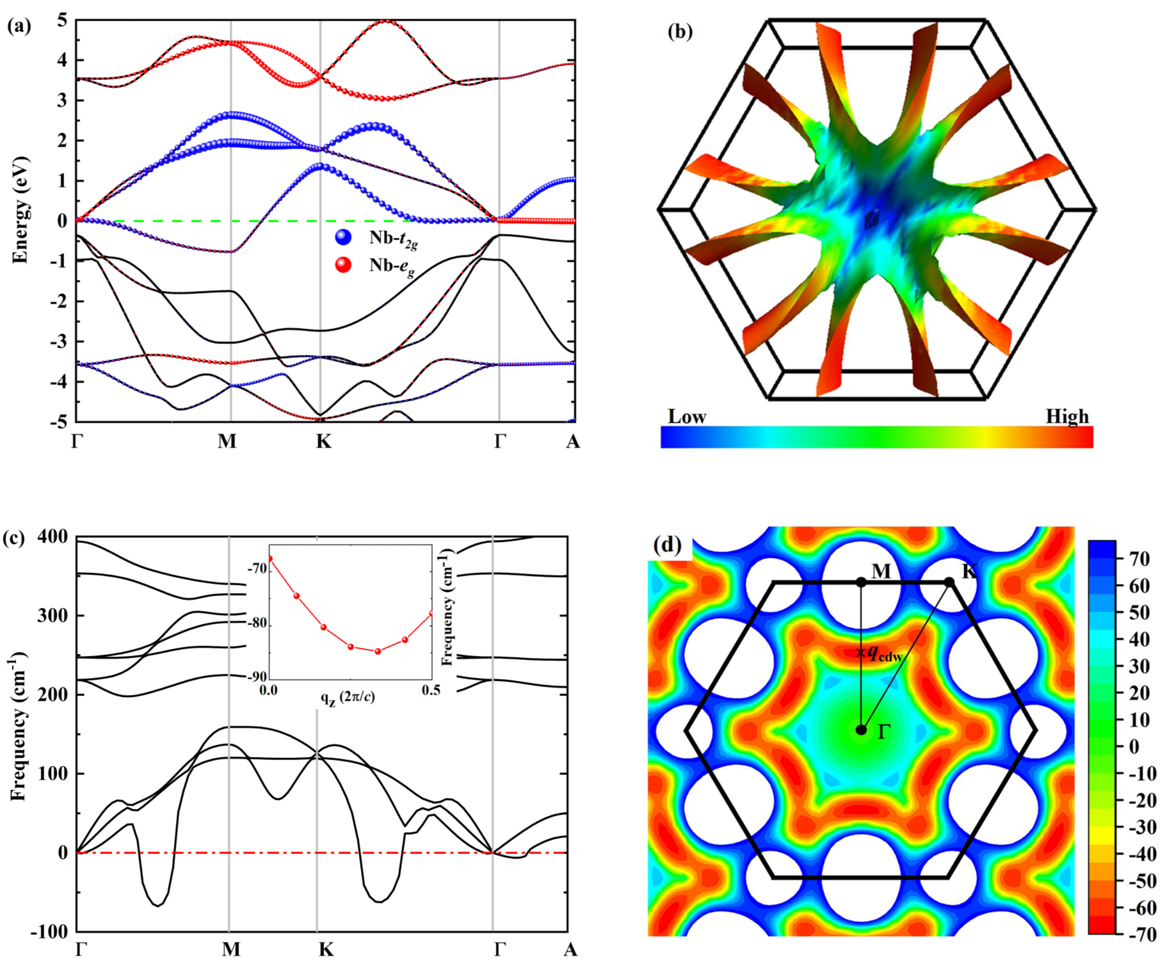

FIG. 2. Electronic structure and phonon spectra of the bulk $1T$-NbS_2 in the high-symmetry phase: (a) band structure, (b) Fermi surface, (c) phonon dispersion curves, and (d) distribution of phonon frequencies at the $q_z = 0$ plane. For the band structure in (a), the dashed line in green color corresponds to the Fermi level ($E_{\rm F}$), and the contributions of Nb t_{2g} (e_g) states are proportional to the size of the blue (red) balls. The color bar of the Fermi surface in (b) denotes the Fermi velocity. Imaginary frequencies in (c) represent unstable modes, and the inset shows the q_z dependence of the unstable acoustic branch. The white regions in (d) indicate phonon frequencies far above 70 cm^{-1}.

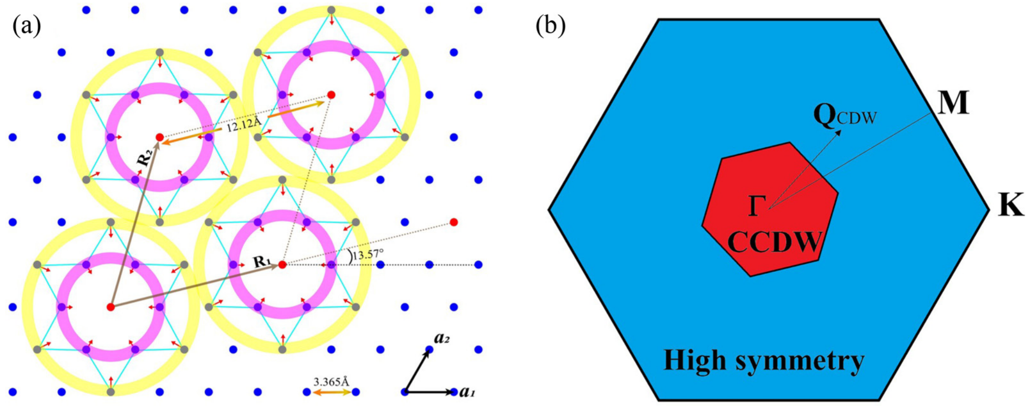

FIG. 3. (a) Schematic illustration of the distortion mode in the Nb-atom layer. The star-of-David clusters are shown in cyan stars. The red arrows illustrate the distortion directions of the Nb atoms. Purple and yellow circles depict the first and second ring of the Nb atoms in the star-of-David cluster, respectively. R_1 and R_2 are lattice vectors of the CCDW phase, whereas a_1 and a_2 are lattice vectors of the high-symmetry phase ($R_1 = 3a_1 + a_2$, $R_2 = -a_1 + 4a_2$). $a^* = 12.12$ Å is the lattice constant of the CCDW phase, while $a = 3.365$ Å is the in-plane lattice constant of the high-symmetry phase. (b) In-plane BZ reconstruction for the CCDW transition. The big blue region represents the first BZ of the high-symmetry phase. The small red hexagon stands for BZ of the CCDW phase. The BZ of the CCDW phase is rotated by 13.57° with respect to that of the high-symmetry phase.

are often characterized by $\boldsymbol{q}_{\mathrm{cdw}} \approx 0.25-0.33 \times \mathbf{\Gamma M}$, depending on the different materials [2,41,58]. In bulk $1T$-NbS_2, the maximally instable acoustic softened mode is located at $\boldsymbol{q}_{\mathrm{cdw}} \approx 0.267 \times \mathbf{\Gamma M}$, which is very close to the ordering vector of $q_{\mathrm{CCDW}} = 1/\sqrt{13} \times \mathbf{\Gamma M}$, the nearest vector along $\mathbf{\Gamma}$-$\mathbf{M}$ compatible with a $\sqrt{13} \times \sqrt{13}$ distortion [16]. This instability persists at all values of q_z, as shown in the inset of Fig. 2(c). Moreover, similar to the $1T$ polymorph of $NbSe_2$ and $TaTe_2$, there is a larger area of instability expanding to the $\mathbf{\Gamma}$-$\mathbf{K}$ line [41,57]. In the $\mathbf{\Gamma}$-$\mathbf{A}$ direction, the flatness of the optical branch implies the almost 2D dispersion, which is in line with the quasi-2D crystal structure of bulk $1T$-NbS_2. We note that the CDW order is absent in $2H$-NbS_2 due to anharmonic suppression, which has been demonstrated by the experimental phonon spectrum and fully anharmonic phonon dispersion curve calculation [23,24]. However, most of the first-principles investigations on the CDW order of TMDCs have not considered the anharmonic effects, but they are still in good agreement with experiments [40,53].

B. Charge density wave phase and orbital density wave of $1T$-NbS_2

After observing the phonon instability for the undistorted high-symmetry phase, we recognize that the high-symmetry structure will undergo a $\sqrt{13} \times \sqrt{13}$ structural reconstruction and transform to a stable CCDW phase with star-of-David clusters. Assuming a nonmagnetic ground state, we perform structural relaxation and obtain the CCDW structure depicted in Fig. 3(a). The $\sqrt{13} \times \sqrt{13}$ superlattice consists of Nb clusters with two shells of six Nb atoms and a central 13th Nb atom coordinated by five kinds of S atoms (detailed atomic positions and the structural mode are presented in Table S1 and Fig. S1 of the Supplemental Material [59]). The lattice constants of the CCDW structure are $a^* = 12.12$ Å and $c^* = 5.97$ Å with space group $P\bar{3}$. As shown in Fig. 3(a), the central Nb atoms keep the same positions relative to the high-symmetry phase, while the peripheral Nb atoms slightly contract toward the central Nb atoms by 5.7% (inner one) and 4.3% (outer one), forming 13-atom star-of-David clusters in the Nb-atom plane, similar to the bulk $1T$-TaS_2 [60]. As shown in Fig. S1 of the Supplemental Material [59], inside of the $\sqrt{13} \times \sqrt{13}$ star-of-David clusters, the distances between two nearest-neighbor Nb atoms are shorter than those in the undistorted $1T$-NbS_2, leading to smaller Nb-S-Nb angles with respect to those of the undistorted phase. Conversely, on the boundary of two star-of-David clusters, the distances of two Nb atoms are longer and the Nb-S-Nb angles are larger. Furthermore, the S atoms outside the plane are affected by the in-plane displacements of Nb atoms, resulting in an out-of-plane buckling, which plays an important role in the orbital hybridization [53]. The in-plane Nb atoms' distortion mode and the corresponding BZ reconstruction are presented in Fig. 3. Due to the lattice distortion, the lattice vectors of the CCDW phase rotate by 13.57° with respect to the high-symmetry phase in real space. Accordingly, as shown in Fig. 3(b), the BZ of the CCDW phase also rotates by 13.57°, resulting in an in-plane $\sqrt{13} \times \sqrt{13}$ R = 13.57° periodic lattice distortion [60]. As shown in Fig. S2 of the Supplemental Material [59], all frequencies of the phonon dispersion for the $\sqrt{13} \times \sqrt{13}$ CCDW phase are positive, revealing that the CCDW phase is dynamically stable, and the nonmagnetic state of the CCDW phase is found to be more stable by 20 meV/NbS_2 with respect to the high-symmetry phase.

The structural distortion of the CCDW phase leads to modifications of the electronic structure. Compared with the band structures of the high-symmetry phase, we find significant changes around E_F in the CCDW phase. As shown in Fig. 4(a), the band structure shows a remarkable in-plane gap of about 0.40 eV, which displays a very weak dispersion (flatband characteristic) along the in-plane $\mathbf{\Gamma}$-$\mathbf{M}$-$\mathbf{K}$-$\mathbf{\Gamma}$ direction but a strong out-of-plane dispersion along the $\mathbf{\Gamma}$-$\mathbf{A}$ direction. In contrast to the quasi-2D flower-shaped Fermi surface of the high-symmetry phase, the CCDW phase exhibits a pair of

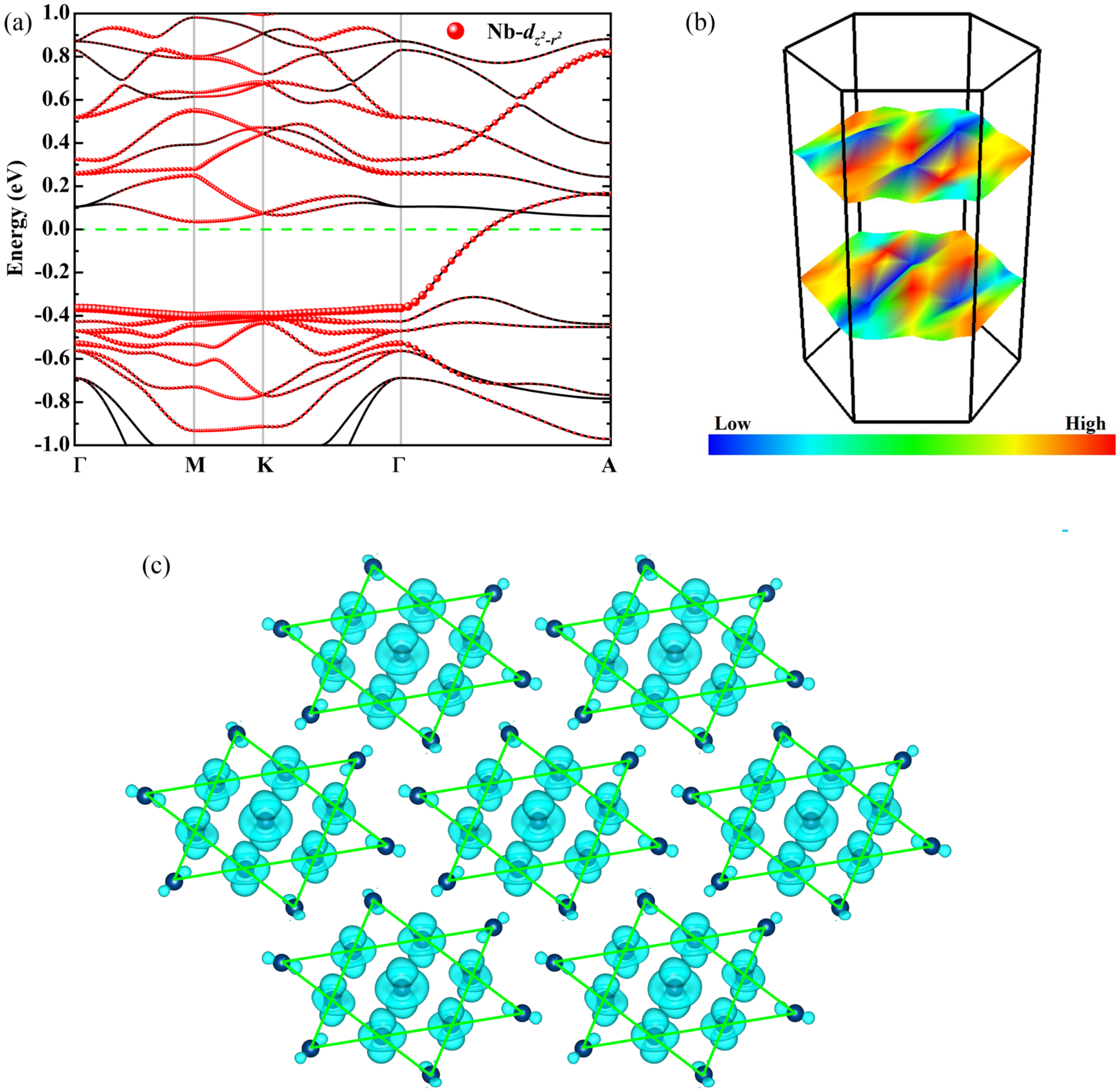

FIG. 4. Electronic structures of the bulk $1T$-NbS_2 in the CCDW phase. (a) Band structure calculated within GGA, where the red balls represent orbital contributions with the $d_{z^2-r^2}$ character. (b) Fermi surface of the CCDW phase, where the color bar denotes the Fermi velocity. (c) The charge density distribution of the uppermost occupied states in real space; the isosurface value is 0.002 electrons/Å^3.

quasi-1D Fermi sheets [Fig. 4(b)]. Such a feature of the electronic structure can be described as an 1D metal, which is in agreement with previous first-principles results for other bulk $1T$ polymorphs such as TaS_2 and $TaSe_2$ [12,16,53]. The in-plane flatband characteristics imply heavy effective masses and small in-plane Fermi velocities; therefore in-plane hopping is difficult for the electrons. The CCDW phase of the $1T$-NbS_2 can be viewed as an in-plane semiconductor [6]. The out-of-plane metallic transport property and the resistivity anisotropy have been revealed by highly accurate in-plane and out-of-plane electrical resistivity measurements for bulk $1T$-TaS_2 [61]. Therefore the transport property of bulk $1T$-NbS_2 at low temperatures deserves further experimental measurement.

Furthermore, an interesting orbital texture within the *ab* plane emerges which is intertwined with the CCDW [6,26,53]. The projected band structures and real-space charge density distributions illustrate that the highest occupied band arises dominantly from the Nb-4d orbitals with $d_{z^2-r^2}$ character, as shown in Fig. S3 of the Supplemental Material [59] and Fig. 4(c). Such an orbital configuration is derived mainly from the inner Nb atoms in the star-of-David clusters. The contribution from the Nb atoms at the edge of the clusters is negligible. Therefore an orbital-density-wave order coexists with the CDW order, which is similar to the in-plane orbital texture of the $1T$ polymorph of TaS_2 and $TaSe_2$ [6,26,53]. The ODW and the CCDW coexist simultaneously with an identical spatial symmetry. The ODW indicates very little in-plane overlap between orbitals centered on neighboring clusters, while charge can only hop significantly along the layer stacking direction (c axis), in agreement with the in-plane flatband characteristics and out-of-plane quasi-1D metallic nature of the electronic structure. The ODW discussed here is different from the orbital ordering studied extensively in strongly correlated electron systems [62]. The conventional orbital ordering stems mainly from the cooperative Jahn-Teller distortions or Kugel-Khomskii superexchange interactions [63,64], whereas the CCDW and the ODW in $1T$ polymorph of MX_2 are mainly attributed to electron-phonon coupling interactions [6,53].

C. Possibility of metal-insulator transition in the CCDW phase

The metal-insulator transition accompanied by the CCDW transition had been observed in the archetypal CDW system, $1T$-TaS_2. However, the origins of the insulating phase and metal-insulator transition are still under extensive debate and have attracted huge interest [7,8,61]. It would be interesting to explore the possibility of realization metal-insulator transition by investigating the electronic correlation interactions and magnetic ordering in the CCDW phase of $1T$-NbS_2. We calculate the electronic structure within spin-polarized GGA for the CCDW phase. Relative to the non-spin-polarized results, the energy is only lowered by a tiny value of 0.06 meV/NbS_2 within spin-polarized calculations. The small energy difference implies that the electronic correlation effect is not the essential reason for the distortion to the CCDW phase, which is consistent with the broad bandwidth of the Nb-4d bands in Fig. 2(a). Furthermore, the spin-up and spin-down subbands are identical to each other (Fig. S3 in the Supplemental Material [59]), and magnetic moment does not appear, implying the CCDW phase is still essentially a nonmagnetic state. Even though the Coulomb correlation effect and spin-orbit coupling (SOC) interactions are taken into account, the CCDW phase remains nonmagnetic metal. As shown in Fig. S3 of the Supplemental Material [59], although the in-plane gap has been enlarged by the on-site electron-electron interaction U, there is still no trace of magnetic behavior, indicating that it is hard to generate an energy splitting for the two spin channels and to realize a magnetic ordering state in the CCDW phase. In addition, SOC interactions have only minor impact on the electronic structures, so it is hard to change the out-of-plane metallic transport property and the nonmagnetic state [12,40,53].

In the CCDW phase of the $1T$-NbS_2, each cluster is constituted by 13 Nb atoms and 26 S atoms, implying that there is one isolated 4d electron in every star-of-David cluster. Such an electronic configuration can create a half-filled band, and it results in a metallic behavior when the Coulomb correction is absent. In fact, no matter whether the spin-polarized, Coulomb correction or SOC interaction have been considered or not, the insulating property or magnetic behavior does not appear based on a $1 \times 1 \times 1$ unit cell of the CCDW phase (Fig. S3 of the Supplemental Material [59]). The metallic behavior of the CCDW phase solely arises from the out-of-plane dispersion, where the interlayer coupling effect delocalizes the in-plane states and suppresses the spin polarization, finally leading to a nonmagnetic ground state [12,65].

However, if the stacking of layers doubles the cell of the CCDW phase, the insulating state can be expected by including an even number of orbitals. Therefore we construct a $1 \times 1 \times 2$ supercell by doubling the cell of the CCDW phase along the layer stacking direction and artificially assign an interlayer AFM ordering by setting an antiparallel magnetic moments direction in near-neighbor layers. Unfortunately,

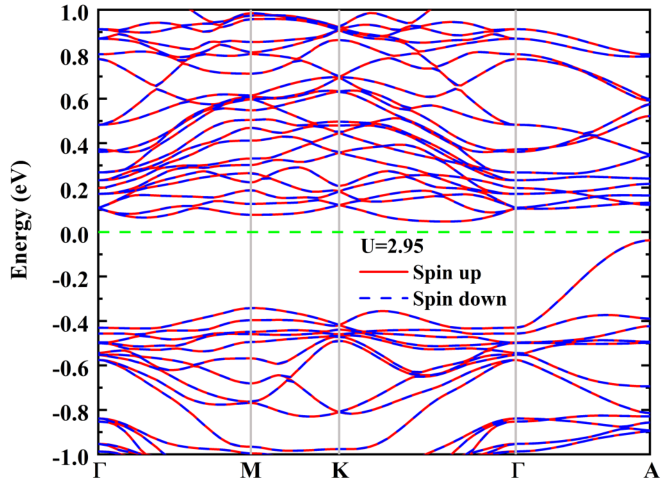

FIG. 5. Electronic band structure of the AFM $\sqrt{13} \times \sqrt{13}$ CCDW phase calculated using a $1 \times 1 \times 2$ supercell within GGA+U.

without Coulomb corrections the system does not favor AFM order and still converges to the nonmagnetic metallic state. Only when AFM ordering and Coulomb corrections have been included simultaneously can a tiny band gap be opened up (Fig. 5 and Fig. S4 of the Supplemental Material [59]). Similar to the monolayer $1T$-NbS_2 [42], the magnetic moments almost arise from the central Nb atoms of the cluster, whereas the contributions from the edge of the star-of-David cluster are negligible.

Previous theoretical investigations show that the monolayer $1T$-TaS_2 is a ferromagnetic (FM) Mott insulator, and the bilayer is an interlayer AFM insulator in the CCDW phase, whereas the ground state of the bulk phase depends on U_{eff}/W (U_{eff} is the effective Coulomb correlation and W is the out-of-plane bandwidth) [12,53]. Coulomb interaction is indispensable to describe the ground state of the CCDW system. For the case of $1T$-NbS_2, there is one isolated 4d electron in every star-of-David cluster of the CCDW phase. According to conventional band theory, an odd-number electron should form a half-filled band, resulting in a metallic behavior without the consideration of the on-site electronic correlation. As shown in Fig. S4 of the Supplemental Material [59], the metallic behavior of the CCDW phase preserves up to a moderate Coulomb correlation of 2 eV. Along with increasing electronic correlation, the Mott gap is opened up and the metal-insulator transition is observed. Nevertheless, we should aware that the energy difference between the insulating AFM state and the metallic nonmagnetic state is only about 0.5 meV/NbS_2 ($U = 2.95$ eV), indicating that the critical temperature for the out-of-plane AFM ordering is very low. Therefore it would be interesting to further clarify the existence of this insulating magnetic ordering state in bulk $1T$-NbS_2 at low temperatures by magnetic property characterization and transport property measurement.

When the dimensionality reduces to the monolayer limit, a previous study has shown that the FM Mott insulating states can emerge in the CCDW phase of the $1T$-MX_2, attributed to be a consequence of the 2D geometry [12,13,40–42,65].

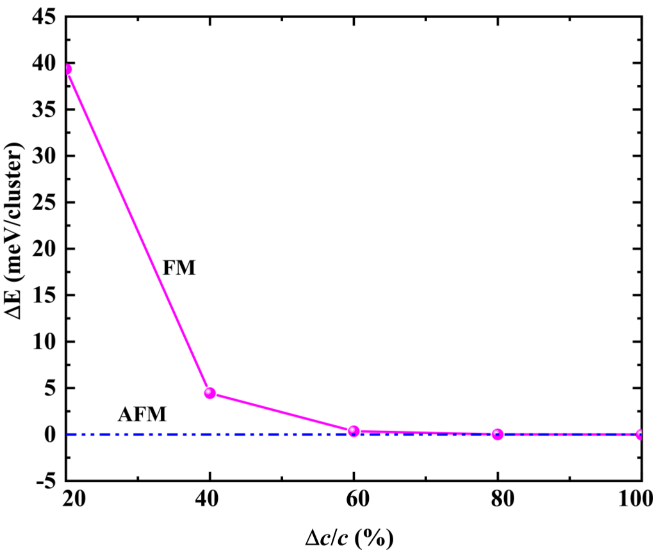

FIG. 6. Energy differences between FM and AFM states for the CCDW phase along with enlarging interlayer distance ($\Delta c/c$, where c is the lattice constant along the layer stacking direction). The calculations are carried out for the $\sqrt{13} \times \sqrt{13}$ CCDW phase within the $1 \times 1 \times 2$ supercell by GGA + U($U = 2.95$ eV).

Recent theoretical predictions pointed out that the CCDW phase of the single-layer $1T$-NbS_2 exhibits a FM insulating nature [42]. However, we find a preset FM state converges to an interlayer AFM solution for the bulk $1T$-NbS_2 with CCDW order, indicating that AFM ordering is a more reasonable ground state. We further inspect the role of the interlayer coupling interactions and the reduced dimensionality by enlarging the interlayer distance. As shown in Fig. 6, the FM state is unstable with higher energy relative to the AFM state, but the energy differences between them reduce rapidly along with increasing interlayer distance. Obviously, the energies almost become the same when the interlayer distances are enlarged by up to 60%. The interlayer coupling interactions become weaker and weaker. Finally, the system becomes essentially identical to the monolayer and a FM insulating state is realized in the monolayer limit [42]. The manipulations of transport properties and magnetic behavior by stacking manner of interlayer, interlayer distances, and intercalation deserve further study.

D. Mechanism of CDW transition and pressure-induced superconductivity

It has been thought that Fermi-surface nesting is one of the driving mechanisms of CDW order [2,3]. A quantitative evaluation of Fermi-surface nesting can be realized by calculating the electron susceptibility or the Fermi-surface nesting function [11]. The nesting function is the low-frequency limit of the imaginary part Im[$\chi_0(\boldsymbol{q})$] of the bare electronic susceptibility in the constant matrix element approximation, whereas the real part Re[$\chi_0(\boldsymbol{q})$] of the bare electronic susceptibility determines the stability of the electronic system. Therefore if the CDW order originates from the Fermi-surface nesting, peaks will appear simultaneously in both of Im[$\chi_0(\boldsymbol{q})$] and

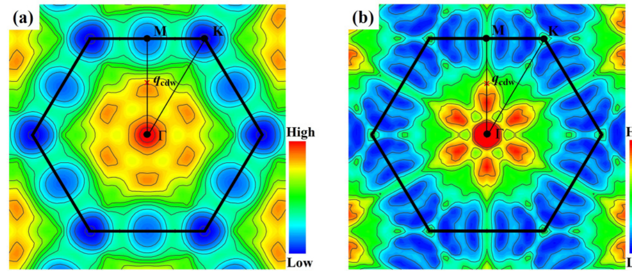

FIG. 7. (a) Real and (b) imaginary parts of the electron susceptibility cross section in the plane of $q_z = 0$ for the high-symmetry bulk $1T$-NbS_2, where $\boldsymbol{q}_{\rm cdw}$ is indicated by the crosses. The color bars denote the relative value.

Re[$\chi_0(\boldsymbol{q})$] at the $\boldsymbol{q}_{\rm cdw}$ [10,11]. The real and imaginary parts of the electron susceptibility are defined as

$$\mathrm{Re}[\chi_0(\boldsymbol{q})] = \sum_k \frac{f(\varepsilon_k) - f(\varepsilon_k)}{\varepsilon_k - \varepsilon_{k+\boldsymbol{q}}}, \tag{1}$$

$$\mathrm{Im}[\chi_0(\boldsymbol{q})] = \sum_k \delta(\varepsilon_k - \varepsilon_F)\delta(\varepsilon_{k+\boldsymbol{q}} - \varepsilon_F), \tag{2}$$

where $f(\varepsilon_k)$ is the Fermi-Dirac function, ε_k are the corresponding Kohn-Sham energies, and ε_F is the Fermi level.

For the undistorted bulk $1T$-NbS_2, a grid of $18 \times 18 \times 9$ k-points is used to calculate the DFT eigenvalues for further evaluation of the electron susceptibility. Then the DFT results are used to construct a tight-binding (TB) model Hamiltonian with the maximally localized Wannier functions (MLWF) method using the WANNIER90 code [66,67]. As shown in Fig. 2(a), the d-like bands split off from the p-like bands by an obvious gap around the Fermi level. Therefore the TB Hamiltonian is constructed with five Nb-4d orbitals. The bands derived from the five-orbital model perfectly match the DFT bands of the bulk $1T$-NbS_2 in the high-symmetry phase (Fig. S5 of the Supplemental Material [59]). Subsequently, the resulting TB Hamiltonian is used to calculate the bare electron susceptibility [68–71]. Although the imaginary part of the electron susceptibility shows a maximum around the $\boldsymbol{\Gamma}$ point, which is owing to intraband contributions from a weakly dispersing band, this is irrelevant for the nesting [72,73]. Both of the real and imaginary parts of the susceptibility show no maxima at the positions of $\boldsymbol{q}_{\rm cdw}$ (Fig. 7). Consequently, the Fermi-surface nesting cannot account for the CDW instability in bulk $1T$-NbS_2.

In addition to the Fermi-surface nesting mechanism, many researchers argue that the momentum-dependent electron-phonon interactions are required to explain the phonon mode softening and create CDW in quasi-2D TMDC systems [2,5,9–11]. The phonon linewidth reflects the strength of the EPC, which does not depend on the positive or imaginary nature of the phonon frequency [15,73]. The calculated phonon linewidth of the lowest phonon mode in the $q_z = 0$ plane indicates that $\boldsymbol{q}_{\rm cdw}$ is in the area with the maximum (Fig. S6 of the Supplemental Material [59]), signifying the EPC may play an important role in CDW formation in $1T$-NbS_2. Furthermore, even though it is problematic to calculate the quantitative EPC of the undistorted phase due to the imaginary frequencies around $\boldsymbol{q}_{\rm cdw}$, it is reasonable to eliminate the imaginary fre-

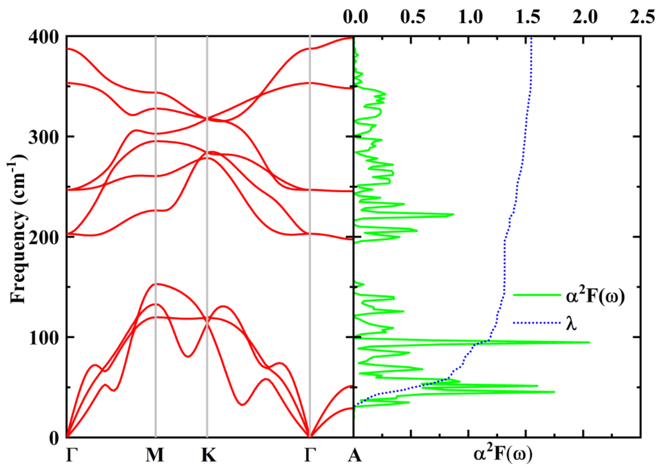

FIG. 8. Phonon dispersion curves and Eliashberg EPC spectral function $\alpha^2F(\omega)$ with the integrated EPC constants λ for the high-symmetry phase of 1T-NbS_2 calculated within a large smearing parameter σ of 0.03 Ry.

quencies of the phonon by increasing the electronic smearing parameter σ during the calculation procedure of the phonon dispersion [74–76]. An electronic smearing of 0.03 Ry is used to stabilize the undistorted bulk 1T-NbS_2 so that the unstable CDW-related acoustic branches can be involved in EPC calculation. The smearing parameter has been carefully verified by relaxation the crystal structure and calculating the electronic band structures of the undistorted phase. As shown in Fig. 8 and Fig. S7 of the Supplemental Material [59], larger σ indeed removes the imaginary phonon mode, and the CDW instability is maintained as shown by the abnormal dip phonons around $\boldsymbol{q}_{\rm cdw}$, whereas the smearing parameter plays almost no role in the lattice constants and band structures [74]. The EPC constant can be calculated by

$$\lambda = 2\int_0^\infty \frac{\alpha^2F(\omega)}{\omega}d\omega, \tag{3}$$

where $\alpha^2F(\omega)$ is the Eliashberg spectral function defined as

$$\alpha^2F(\omega) = \frac{1}{2\pi N(E_{\rm F})}\sum_q \delta(\omega-\omega_q)\frac{\gamma_q}{\hbar\omega_q}, \tag{4}$$

where $N(E_{\rm F})$ is the DOS at Fermi level and $\gamma_{\rm q}$ is the phonon linewidth. The EPC constant is calculated to be as large as 1.55, indicating that the CDW instability of bulk 1T-NbS_2 is mainly attributed to softened phonon arising from strong EPC interactions. The indispensable role of EPC in driving the CDW transition has been recognized in the 1T polymorph of $TaSe_2$ and TaS_2 [15,16].

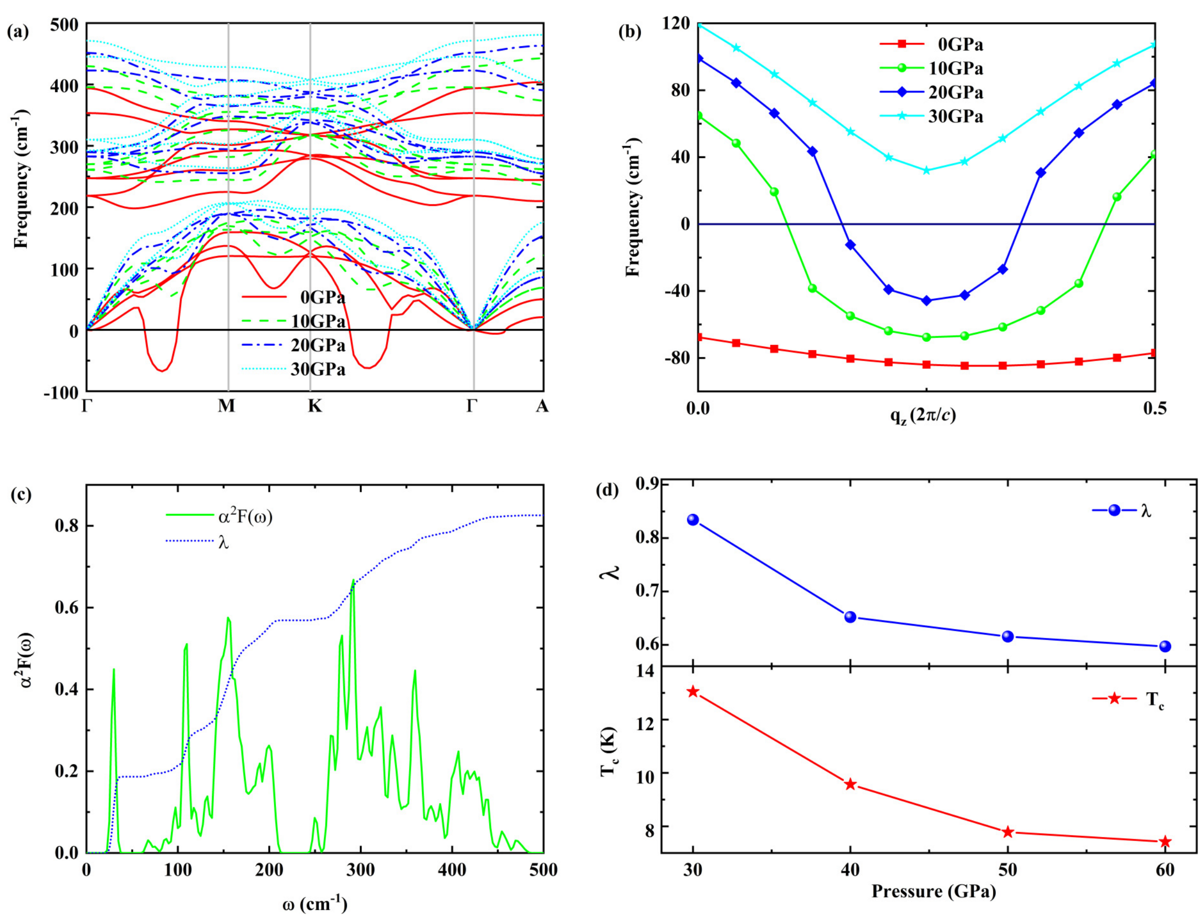

FIG. 9. Evolution of (a) phonon dispersion and (b) q_z dependence of the unstable acoustic branch of 1T-NbS_2 under high pressure. (c) Eliashberg spectral function $\alpha^2F(\omega)$ and the EPC integral λ(ω) at pressure of 30 GPa. (d) The evolutions of EPC constants (λ) and superconducting temperatures (T_c) of compressed 1T-NbS_2.

Previous studies show that it is possible to suppress the CDW instability upon applying pressure and trigger superconductivity in $1T$-MX_2 [13,15–19,57]. As shown in Fig. 9(a), the unstable modes in the bulk of $1T$-NbS_2 gradually harden with increasing pressure. The unstable phonon modes of the high-symmetry structure will disappear completely, and a stable phase appears above the pressure of 30 GPa [Fig. 9(b)]. In order to inspect the relationship between the electron-lattice interaction and the CDW instability, we have calculated the EPC constants as a function of pressure in the high-symmetry phase. Along with increasing pressures, where the $1T$ structure becomes stable, $\alpha^2F(\omega)$ shows an obvious change with a sharp decrease of its intensity, leading to a remarkable reduction of the EPC constant from 1.55 down to 0.82 as the CDW instability is suppressed [Fig. 9(c)]. Accompanied by the suppression of the CDW order, the superconductivity can emerge in the bulk of $1T$-NbS_2. The superconducting transition temperature T_c is estimated by the Allen-Dynes–modified McMillan formula [77,78]:

$$T_c = \frac{\omega_{\log}}{1.2} \exp\left(-\frac{1.04(1+\lambda)}{\lambda - \mu^* - 0.62\lambda\mu^*}\right), \tag{5}$$

where the Coulomb pseudopotential μ^* is assumed to be 0.1, λ is the EPC constant defined in Eq. (3), and $\omega_{\log}$ is the logarithmic average frequency:

$$\omega_{\log} = \exp\left(\frac{2}{\lambda}\int \frac{\log\omega}{\omega}\alpha^2F(\omega)d\omega\right), \tag{6}$$

with the Eliashberg spectral function $\alpha^2F(\omega)$ defined in Eq. (4).

At pressure of 30 GPa, the superconducting transition temperature T_c is estimated to be 13.05 K, which is larger than those of the $1T$ polymorph of TaS_2 and $TaSe_2$ as well as their doping compounds $TaS_{1-x}Se_x$ [17–19]. As the CDW instability is just suppressed and the system enters into the superconducting phase, the original imaginary frequency becomes positive, resulting in large λ and high T_C. The EPC constants and superconducting transition temperatures of the compressed $1T$-NbS_2 decrease monotonously along with the increasing pressure [Fig. 9(d)]. The downward trend of the superconducting transition temperatures with increasing pressure is in qualitative agreement with previous theoretically predicted results of the $1T$ polymorph of TaS_2 and $TaSe_2$ [15,16]. Generally, pressure-induced lattice deformation directly causes an enhancement of $N(E_F)$ at the Fermi level and the instability of phonon vibration modes. Electronic structure calculations indicate a tiny decrease of $N(E_F)$ along with the increasing pressure, whereas the phonons of the compressed superconducting phase display an overall blueshift compared to the ambient pressure phase $1T$-NbS_2 (Fig. S8 of the Supplemental Material [59]). Pressure compresses the lattice volume and the phonon spectra gradually harden, which leads to the reduction of λ and a consequent decrease of the superconducting transition temperature.

It should be aware that superconductivity and CDW order are not absolutely exclusive with each other. Although CDW instability in pristine $1T$-TaS_2 has been predicted theoretically to be suppressed by high pressure [15], the coexistence of pressure-induced superconductivity with CDW order has been observed experimentally above 4 GPa [13,17–19]. The superconductivity and its coexistence with CDW order under high pressure have been explained in terms of a microscopic phase separation in real space [13]. As shown in Fig. 9, the phonon spectrum gradually hardens with increasing pressure. The in-plane imaginary phonon modes have disappeared above 10 GPa, but the q_z dependence of the unstable acoustic branch remains negative until the pressure increases up to 30 GPa. In addition, anomalies in the acoustic branches along the **Γ-M** and **Γ-K** directions persist, signaling the incipient CDW instability of the high-symmetry $1T$-NbS_2 even up to 30 GPa [15,16]. We suspect that the CDW order may coexist with the superconducting state until the thorough suppression of the CDW instability by pressure, and the coexistence of CDW order with superconductivity could be a possible phase for this system. Further experimental studies on $1T$-NbS_2 under pressure can give us the details and address this issue.

IV. CONCLUSIONS

By employing first-principles calculation, we predict that bulk $1T$-NbS_2 is unstable due to a softened phonon mode and will transform to a stable CCDW phase with a $\sqrt{13} \times \sqrt{13}$ structural reconstruction. Electronic structure calculation suggests that the ODW can coexist with the CDW order in the CCDW phase. A metal-insulator transition can be realized in the CCDW phase, provided that the interlayer AFM ordering and the Coulomb correlation effect are taken into account simultaneously. Bare electron susceptibility, phonon linewidth, and EPC constant calculations suggest that the EPC interactions account for the CDW instability. Furthermore, the CDW order can be suppressed by high pressure, and superconductivity emerges in the compressed structure with moderate EPC interactions. Our theoretical predictions call for further experimental study of the electronic structure and magnetic properties of the $1T$-NbS_2. Moreover, it will be interesting to study the possibility of coexistence of CDW order and superconductivity in $1T$-NbS_2.

ACKNOWLEDGMENTS

The authors would like to thank Chao Cao, Wenjian Lu, Chenchao Xu, Pengfei Liu, Jianyong Chen, and Yunhai Li for inspiring discussions and valuable suggestions. This work was sponsored by the National Natural Science Foundation of China (Grants No. 11864008 and No. 11704084) and the Guangxi Natural Science Foundation (Grants No. 2018GXNSFAA138185, No. 2018AD19200 and No. 2019GXNSFGA245006). C.A. is supported by the Foundation for Polish Science through the International Research Agendas program, cofinanced by the European Union within the Smart Growth Operational Program. Z.G. acknowledges financial support from MOE tier 1 funding of the Singapore (Grant No. R-144-000-402-114).

[1] H. Yang, S. Kim, M. Chhowalla, and Y. H. Lee, Structural and quantum-state phase transitions in van der Waals layered materials, Nat. Phys. **13**, 931 (2017).

[2] X. Zhu, Y. Cao, J. Zhang, E. W. Plummer, and J. Guo, Classification of charge density waves based on their nature, Proc. Natl. Acad. Sci. USA **112**, 2367 (2015).

[3] J. A. Wilson, F. J. Di Salvo, and S. Mahajan, Charge-Density Waves in Metallic, Layered, Transition-Metal Dichalcogenides, Phys. Rev. Lett. **32**, 882 (1974).

[4] A. H. Castro Neto, Charge Density Wave, Superconductivity, and Anomalous Metallic Behavior in 2D Transition Metal Dichalcogenides, Phys. Rev. Lett. **86**, 4382 (2001).

[5] K. Rossnagel, On the origin of charge-density waves in select layered transition-metal dichalcogenides, J. Phys.: Condes. Matter **23**, 213001 (2011).

[6] T. Ritschel, J. Trinckauf, K. Koepernik, B. Büchner, M. v. Zimmermann, H. Berger, Y. I. Joe, P. Abbamonte, and J. Geck, Orbital textures and charge density waves in transition metal dichalcogenides, Nat. Phys. **11**, 328 (2015).

[7] C. J. Butler, M. Yoshida, T. Hanaguri, and Y. Iwasa, Mottness versus unit-cell doubling as the driver of the insulating state in $1T$-TaS_2, Nat. Commun. **11**, 2477 (2020).

[8] S. H. Lee, J. S. Goh, and D. Cho, Origin of the Insulating Phase and First-Order Metal-Insulator Transition in $1T$-TaS_2, Phys. Rev. Lett. **122**, 106404 (2019).

[9] T. M. Rice and G. K. Scott, New Mechanism for a Charge-Density-Wave Instability, Phys. Rev. Lett. **35**, 120 (1975).

[10] M. D. Johannes, I. I. Mazin, and C. A. Howells, Fermi-surface nesting and the origin of the charge-density wave in $NbSe_2$, Phys. Rev. B **73**, 205102 (2006).

[11] M. D. Johannes and I. I. Mazin, Fermi surface nesting and the origin of charge density waves in metals, Phys. Rev. B **77**, 165135 (2008).

[12] P. Darancet, A. J. Millis, and C. A. Marianetti, Three-dimensional metallic and two-dimensional insulating behavior in octahedral tantalum dichalcogenides, Phys. Rev. B **90**, 045134 (2014).

[13] B. Sipos, A. F. Kusmartseva, A. Akrap, H. Berger, L. Forró, and E. Tutiš, From Mott state to superconductivity in $1T$-TaS_2, Nat. Mater. **7**, 960 (2008).

[14] K. Horiba, K. Ono, J. H. Oh, T. Kihara, S. Nakazono, M. Oshima, O. Shiino, H. W. Yeom, A. Kakizaki, and Y. Aiura, Charge-density wave and three-dimensional Fermi surface in $1T$-$TaSe_2$ studied by photoemission spectroscopy, Phys. Rev. B **66**, 073106 (2002).

[15] A. Y. Liu, Electron-phonon coupling in compressed $1T$-TaS_2: Stability and superconductivity from first principles, Phys. Rev. B **79**, 220515 (2009).

[16] Y. Ge and A. Y. Liu, First-principles investigation of the charge-density-wave instability in $1T$-$TaSe_2$, Phys. Rev. B **82**, 155133 (2010).

[17] B. Wang, Y. Liu, K. Ishigaki, K. Matsubayashi, J. Cheng, W. J. Lu, Y. P. Sun, and Y. Uwatoko, Pressure-induced bulk superconductivity in a layered transition-metal dichalcogenide 1T - tantalum selenium, Phys. Rev. B **95**, 220501 (2017).

[18] T. Ritschel, J. Trinckauf, G. Garbarino, M. Hanfland, M. v. Zimmermann, H. Berger, B. Büchner, and J. Geck, Pressure dependence of the charge density wave in $1T$-TaS_2 and its relation to superconductivity, Phys. Rev. B **87**, 125135 (2013).

[19] B. Wang, Y. Liu, X. Luo, K. Ishigaki, K. Matsubayashi, W. J. Lu, Y. P. Sun, J. G. Cheng, and Y. Uwatoko, Universal phase diagram of superconductivity and charge density wave versus high hydrostatic pressure in pure and Se-doped $1T$-TaS_2, Phys. Rev. B **97**, 220504 (2018).

[20] D. C. Freitas, P. Rodière, M. R. Osorio, E. Navarro-Moratalla, N. M. Nemes, V. G. Tissen, L. Cario, E. Coronado, M. García-Hernández, S. Vieira, M. Núñez-Regueiro, and H. Suderow, Strong enhancement of superconductivity at high pressures within the charge-density-wave states of 2H-TaS_2 and 2H-$TaSe_2$, Phys. Rev. B **93**, 184512 (2016).

[21] T. Kiss, T. Yokoya, A. Chainani, S. Shin, T. Hanaguri, M. Nohara, and H. Takagi, Charge-order-maximized momentum-dependent superconductivity, Nat. Phys. **3**, 720 (2007).

[22] R. Grasset, Y. Gallais, A. Sacuto, M. Cazayous, S. Mañas-Valero, E. Coronado, and M. A. Méasson, Pressure-Induced Collapse of the Charge Density Wave and Higgs Mode Visibility in 2H-TaS_2, Phys. Rev. Lett. **122**, 127001 (2019).

[23] M. Leroux, M. Le Tacon, M. Calandra, L. Cario, M.-A. Méasson, P. Diener, E. Borrissenko, A. Bosak, and P. Rodière, Anharmonic suppression of charge density waves in 2H-NbS_2, Phys. Rev. B **86**, 155125 (2012).

[24] C. Heil, S. Poncé, H. Lambert, M. Schlipf, E. R. Margine, and F. Giustino, Origin of Superconductivity and Latent Charge Density Wave in NbS_2, Phys. Rev. Lett. **119**, 087003 (2017).

[25] M. Leroux, L. Cario, A. Bosak, and P. Rodière, Traces of charge density waves in NbS_2, Phys. Rev. B **97**, 195140 (2018).

[26] Y. Chen, W. Ruan, M. Wu, S. J. Tang, H. Ryu, H. Z. Tsai, R. Lee, S. Kahn, F. Liou, C. H. Jia, O. R. Albertini, H. Y. Xiong, T. Jia, Z. Liu, J. A. Sobota, A. Y. Liu, J. E. Moore, Z. X. Shen, S. G. Louie, S.-K. Mo, and M. F. Crommie, Strong correlations and orbital texture in single-layer $1T$-$TaSe_2$, Nat. Phys. **16**, 218 (2020).

[27] H. C. Lin, W. T. Huang, K. Zhao, S. Qiao, Z. Liu, J. Wu, X. Chen, and S. H. Ji, Scanning tunneling spectroscopic study of monolayer $1T$-TaS_2 and $1T$-$TaSe_2$, Nano Res. **13**, 133 (2020).

[28] H. Lin, W. Huang, K. Zhao, C. Lian, W. Duan, X. Chen, and S. H. Ji, Growth of atomically thick transition metal sulfide films on graphene/6H-SiC (0001) by molecular beam epitaxy, Nano Res. **11**, 4722 (2018).

[29] R. M. Stan, S. K. Mahatha, M. Bianchi, C. E. Sanders, D. Curcio, P. Hofmann, and J. A. Miwa, Epitaxial single-layer NbS_2 on Au (111): Synthesis, structure, and electronic properties, Phys. Rev. Mater. **3**, 044003 (2019).

[30] R. Bianco, I. Errea, L. Monacelli, M. Calandra, and F. Mauri, Quantum enhancement of charge density wave in NbS_2 in the two-dimensional limit, Nano Lett. **19**, 3098 (2019).

[31] F. Cossu, K. Palotás, S. Sarkar, I. Di Marco, and A. Akbari, Strain-induced stripe phase in charge-ordered single layer $NbSe_2$, NPG Asia Mater. **12**, 24 (2020).

[32] X. Xi, L. Zhao, Z. Wang, H. Berger, L. Forró, J. Shan, and K. F. Mak, Strongly enhanced charge-density-wave order in monolayer $NbSe_2$, Nat. Nanotechnol. **10**, 765 (2015).

[33] C. S. Lian, C. Heil, X. Liu, C. Si, F. Giustino, and W. Duan, Coexistence of superconductivity with enhanced charge density wave order in the two-dimensional limit of $TaSe_2$, J. Phys. Chem. Lett. **10**, 4076 (2019).

[34] Y. F. Yang, S. A. Fang, V. Fatemi, J. Ruhman, E. Navarro-Moratalla, K. Watanabe, T. Taniguchi, E. Kaxiras, and P. Jarillo-Herrero, Enhanced superconductivity upon weakening

of charge density wave transport in 2H-TaS_2 in the two-dimensional limit, Phys. Rev. B **98**, 035203 (2018).

[35] S. C. de la Barrera, M. R. Sinko, D. P. Gopalan, N. Sivadas, K. L. Seyler, K. Watanabe, T. Taniguchi, A. W. Tsen, X. D. Xu, D. Xiao, and B. M. Hunt, Tuning Ising superconductivity with layer and spin-orbit coupling in two-dimensional transition-metal dichalcogenides, Nat. Commun. **9**, 1427 (2018).

[36] C. J. Carmalt, T. D. Manning, I. P. Parkin, E. S. Peters, and A. L. Hector, Formation of a new (1T) trigonal NbS_2 polytype via atmospheric pressure chemical vapour deposition, J. Mater. Chem. **14**, 290 (2004).

[37] X. Chen, Y. Gu, G. Tao, Y. Pei, G. Wang, and N. Cui, Origin of hydrogen evolution activity on MS_2 (M = Mo or Nb) monolayers, J. Mater. Chem. A **3**, 18898 (2015).

[38] Y. Nakata, K. Sugawara, R. Shimizu, Y. Okada, P. Han, T. Hitosugi, K. Ueno, T. Sato, and T. Takahashi, Monolayer $1T$-$NbSe_2$ as a Mott insulator, NPG Asia Mater. **8**, e321 (2016).

[39] F. Bischoff, W. Auwärter, J. V. Barth, A. Schiffrin, M. Fuhrer, and B. Weber, Nanoscale phase engineering of niobium diselenide, Chem. Mater. **29**, 9907 (2017).

[40] M. Calandra, Phonon-Assisted Magnetic Mott-Insulating State in the Charge Density Wave Phase of Single-Layer $1T$-$NbSe_2$, Phys. Rev. Lett. **121**, 026401 (2018).

[41] D. Pasquier and O. V. Yazyev, Charge density wave phase, Mottness, and ferromagnetism in monolayer $1T$-$NbSe_2$, Phys. Rev. B **98**, 045114 (2018).

[42] C. Tresca and M. Calandra, Charge density wave and spin 1/2 insulating state in single layer $1T$-NbS_2, 2D Mater. **6**, 035041 (2019).

[43] P. Giannozzi, S. Baroni, N. Bonini, M. Calandra, R. Car, C. Cavazzoni, D. Ceresoli, G. L. Chiarotti, M. Cococcioni, I. Dabo, A. D. Corso, S. Gironcoli, S. Fabris, G. Fratesi, R. Gebauer, U. Gerstmann, C. Gougoussis, A. Kokalj, M. Lazzeri, L. Martin-Samos *et al.*, Quantum Espresso: A modular and open-source software project for quantum simulations of materials, J. Phys.: Condes. Matter **21**, 395502 (2009).

[44] J. P. Perdew, K. Burke, and M. Ernzerhof, Generalized Gradient Approximation Made Simple, Phys. Rev. Lett. **77**, 3865 (1996).

[45] D. Vanderbilt, Soft self-consistent pseudopotentials in a generalized eigenvalue formalism, Phys. Rev. B **41**, 7892 (1990).

[46] S. Grimme, Semiempirical GGA-type density functional constructed with a long-range dispersion correction, J. Comput. Chem. **27**, 1787 (2006).

[47] H. J. Monkhorst and J. D. Pack, Special points for Brillouin-zone integrations, Phys. Rev. B **13**, 5188 (1976).

[48] S. Baroni, S. de Gironcoli, A. Dal Corso, and P. Giannozzi, Phonons and related crystal properties from density-functional perturbation theory, Rev. Mod. Phys. **73**, 515 (2001).

[49] G. Kresse and J. Hafner, Ab initio molecular dynamics for liquid metals, Phys. Rev. B **47**, 558 (1993).

[50] G. Kresse and J. Furthmüller, Efficiency of ab-initio total energy calculations for metals and semiconductors using a plane-wave basis set, Comput. Mater. Sci. **6**, 15 (1996).

[51] G. Kresse and D. Joubert, From ultrasoft pseudopotentials to the projector augmented-wave method, Phys. Rev. B **59**, 1758 (1999).

[52] M. Kawamura, FermiSurfer: Fermi-surface viewer providing multiple representation schemes, Comput. Phys. Commun. **239**, 197 (2019).

[53] X. L. Yu, D. Y. Liu, Y. M. Quan, J. Wu, H. Q. Lin, K. Chang, and L. J. Zou, Electronic correlation effects and orbital density wave in the layered compound $1T$-TaS_2, Phys. Rev. B **96**, 125138 (2017).

[54] F. Clerc, C. Battaglia, H. Cercellier, C. Monney, H. Berger, L. Despont, M. G. Garnier, and P. Aebi, Fermi surface of layered compounds and bulk charge density wave systems, J. Phys.: Condes. Matter **19**, 355002 (2007).

[55] M. Bovet, D. Popović, F. Clerc, C. Koitzsch, U. Probst, E. Bucher, H. Berger, D. Naumović, and P. Aebi, Pseudogapped Fermi surfaces of $1T$-TaS_2 and $1T$-$TaSe_2$: A charge density wave effect, Phys. Rev. B **69**, 125117 (2004).

[56] D. F. Shao, R. C. Xiao, W. J. Lu, H. Y. Lv, J. Y. Li, X. B. Zhu, and Y. P. Sun, Manipulating charge density waves in $1T$-TaS_2 by charge-carrier doping: A first-principles investigation, Phys. Rev. B **94**, 125126 (2016).

[57] Y. Liu, D. F. Shao, L. J. Li, W. J. Lu, X. D. Zhu, P. Tong, R. C. Xiao, L. S. Ling, C. Y. Xi, L. Pi, H. F. Tian, H. X. Yang, J. Q. Li, W. H. Song, X. B. Zhu, and Y. P. Sun, Nature of charge density waves and superconductivity in $1T$-$TaSe_{2-x}Te_x$, Phys. Rev. B **94**, 045131 (2016).

[58] A. M. Woolley and G. Wexler, Band structures and Fermi surfaces for $1T$-TaS_2, $1T$-$TaSe_2$ and $1T$-VSe_2, J. Phys. C: Solid State Phys. **10**, 2601 (1977).

[59] See Supplemental Material http://link.aps.org/supplemental/10.1103/PhysRevB.102.155115 for structural parameters, phonon dispersions, bands structures of the CCDW phase, DFT and MLWF bands, phonon linewidth, phonon dispersions, bands structures of the high symmetry phase, phonon dispersions and density of states of the compressed bulk 1T-NbS_2 at different pressure.

[60] O. R. Albertini, R. Zhao, R. L. McCann, S. Feng, M. Terrones, J. K. Freericks, J. A. Robinson, and A. Y. Liu, Zone-center phonons of bulk, few-layer, and monolayer $1T$-TaS_2: Detection of commensurate charge density wave phase through Raman scattering, Phys. Rev. B **93**, 214109 (2016).

[61] E. Martino, A. Pisoni, L. Ćirić, A. Arakcheeva, H. Berger, A. Akrap, C. Putzke, P. J. W. Moll, I. Batistić, E. Tutiš, L. Forró, and K. Semeniuk, Preferential out-of-plane conduction and quasi-one-dimensional electronic states in layered $1T$-TaS_2, npj 2D Mater Appl. **4**, 7 (2020).

[62] Y. Tokura and N. Nagaosa, Orbital physics in transition-metal oxides, Science **288**, 462 (2000).

[63] J. Kanamori, Crystal distortion in magnetic compounds, J. Appl. Phys. **31**, S14 (1960).

[64] K. I. Kugel and D. I. Khomskii, Crystal-structure and magnetic properties of substances with orbital degeneracy, Sov. Phys. JETP **37**, 725 (1973).

[65] Q. Zhang, L. Y. Gan, Y. Cheng, and U. Schwingenschlögl, Spin polarization driven by a charge-density wave in monolayer $1T$-TaS_2, Phys. Rev. B **90**, 081103 (2014).

[66] N. Marzari and D. Vanderbilt, Maximally localized generalized Wannier functions for composite energy bands, Phys. Rev. B **56**, 12847 (1997).

[67] A. A. Mostofi, J. R. Yates, Y. S. Lee, I. Souza, D. Vanderbilt, and N. Marzari, Wannier90: A tool for obtaining maximally-

localised Wannier functions, Comput. Phys. Commun. **178**, 685 (2008).

[68] C. C. Xu, Q. J. Chen, and C. Cao, Unique crystal field splitting and multiband RKKY interactions in Ni-doped $EuRbFe_4As_4$, Commun. Phys. **2**, 16 (2019).

[69] H. Chen, X. Xu, C. Cao, and J. Dai, First-principles calculations of the electronic and phonon properties of APt_3P (A = Ca, Sr, and La): Evidence for a charge-density-wave instability and a soft phonon, Phys. Rev. B **86**, 125116 (2012).

[70] H. Jiang, G. H. Cao, and C. Cao, Electronic structure of quasi-one-dimensional superconductor $K_2Cr_3As_3$ from first-principles calculations, Sci. Rep. **5**, 16054 (2015).

[71] C. Xu, N. Wu, G. X. Zhi, B. H. Lei, X. Duan, F. Ning, C. Cao, and Q. Chen, Coexistence of nontrivial topological properties and strong ferromagnetic fluctuations in quasi-one-dimensional $A_2Cr_3As_3$, npj Comput. Mater. **6**, 30 (2020).

[72] F. Clerc, C. Battaglia, M. Bovet, L. Despont, C. Monney, H. Cercellier, M. G. Garnier, P. Aebi, H. Berger, and L. Forró, Lattice-distortion-enhanced electron-phonon coupling and Fermi surface nesting in $1T$-TaS_2, Phys. Rev. B **74**, 155114 (2006).

[73] J. G. Si, W. J. Lu, H. Y. Wu, H. Y. Lv, X. Liang, Q. J. Li, and Y. P. Sun, Origin of the multiple charge density wave order in $1T$-VSe_2, Phys. Rev. B **101**, 235405 (2020).

[74] F. P. Zheng and J. Feng, Electron-phonon coupling and the coexistence of superconductivity and charge-density wave in monolayer $NbSe_2$, Phys Rev B **99**, 161119 (2019).

[75] N. F. Hinsche and K. S. Thygesen, Electron–phonon interaction and transport properties of metallic bulk and monolayer transition metal dichalcogenideTaS_2, 2D Mater. **5**, 015009 (2017).

[76] D. L. Duong, M. Burghard, and J. C. Schön, Ab initio computation of the transition temperature of the charge density wave transition in $TiSe_2$, Phys. Rev. B **92**, 245131 (2015).

[77] P. B. Allen and R. C. Dynes, Transition temperature of strong-coupled superconductors reanalyzed, Phys. Rev. B **12**, 905 (1975).

[78] R. C. Dynes, McMillan's equation and the T_C of superconductors, Solid State Commun. **10**, 615 (1972).